Journal of Engineering Science and Technology
ICIST2023, Vol. 19, No. 2 (2024) 83 - 97
© School of Engineering, Taylor's University

FLUID-STRUCTURE INTERACTION MODELING FOR VIBRATION ENERGY EXTRACTION FROM A CIRCULAR CYLINDER IN CROSS-FLOW

AVICENNA AN-NIZHAMI[1,*], NANANG APRIANDI[1], ALI SAI'IN[1], PADANG YANUAR[1], WAHYU ISTI NUGROHO[1], ELFRIDA RIZKY RIADINI[2]

[1]Mechanical Engineering Department, Politeknik Negeri Semarang,
Jl. Prof. Sudarto, Tembalang, Kota Semarang, Jawa Tengah, Indonesia, 50275
[2]Mechanical Engineering Department, Universitas Gadjah Mada,
Bulaksumur, Yogyakarta, Indonesia, 55281
*Corresponding Author: avicenna@polines.ac.id

Abstract

Conventional turbines encounter limitations for low-speed flows. To overcome these challenges, have proposed employing the Flow-Induced Vibration (FIV) to induce oscillations in a cylinder exposed to fluid flow. This research aims to numerically examine the impact of Reynolds number (Re), reduced velocity, and damping ratio on the behaviour of a system that uses vibration energy harvesting (VEH) to capture low-speed flow kinetic energy. The research focuses on Reynolds number values ranging from 100 to 500, the reduced velocity (U_R) ranging from 1.0 to 15.0, and three distinct damping ratios (ζ) at 0.05, 0.1, and 0.5. The simulation was performed utilising in-house numerical code based on the finite volume method, while the structural dynamics were solved using the Dormand-Prince method. The Direct Forcing Immersed Boundary method was employed to handle the no-slip boundary condition and calculate the force exerted on the cylinder. The research shows that when the Reynolds number increases, the cylinder's non-dimensional displacement increases, indicating a more intense fluid flow. As Reynolds number increases, so do the cylinder motion's fundamental frequencies. The analysis suggests that cylinder displacement rises with increasing Reynolds numbers, except at 400. Higher Reynolds numbers amplify displacement and advance the cylinder's fundamental frequency of motion. The displacement's root mean square grows with reduced velocity until it peaks. The peak is influenced by the damping ratio. At a damping ratio of 0.1, the peak yielding the highest peak value. The average potential generated power increases with the reduced velocity but varies, particularly at a damping ratio of 0.5.

Keywords: Direct forcing immersed boundary, Flow-induced vibration, Low-speed flow, Potential generated power, Vibration energy harvesting.

1. Introduction

The energy that exists in the environment and nature is not fully transformed into usable energy. One example is the underutilised potential of kinetic energy in motor vehicles. The prospect of transforming this kinetic energy into usable energy sources has been discovered in research by Pan et al. [1]. The vibration energy produced by the dynamics of automobiles can potentially be harvested and used as a source of energy. Research by An-Nizhami et al. [2] explores the use of this vibration energy and its significance in producing electricity to increase the efficiency of electric cars.

Another overlooked energy source is the energy contained in ocean waves. Helpful information on harnessing ocean wave energy for power production can be found in the studies by An-Nizhami and Riadini [3] and Lin and Zhang [4]. Solar energy is another potential energy source. According to research by Sardini and Serpelloni [5], there are several ways to gather solar energy and transform it into a source of usable energy to meet everyday demands.

Wasted thermal energy presents another option for energy harvesting. According to a study by Sebald et al. [6], many techniques can be utilised to capture and utilise wasted thermal energy, including energy regeneration systems and thermal energy collector technologies. Investigating these potentials and developing efficient strategies for converting these energies into usable and sustainable sources would require more research and development. This enable the use of already available energy sources to be maximised.

Water and wind turbines are currently the most widely employed technology in sustainable energy production. These turbines have a speed range of 1.5 to 5 m/s. However, most river and wind flows occur at velocities between 0.3 and 1.0 m/s. This presents a significant challenge to extracting kinetic energy from low-speed flows using conventional turbines.

In order to solve this issue, researchers have proposed a method that uses the Flow-Induced Vibration (FIV) phenomenon. When a cross-flow passes a cylinder, an "FIV" vibration phenomenon occurs. Throughout the process, the surface of the cylinder experiences alternating stresses from the fluid flow, which causes the solid structure to oscillate.

Vibration energy harvesting (VEH) technologies can close the gap in generating low-speed flow kinetic energy by employing the FIV. The VEH converter can effectively capture the energy coming from low-speed water flows, which was previously challenging to harness. VEH devices are capable of converting various vibration sources into electricity using a variety of different mechanisms.

With the help of an electromagnetic interaction between the magnetic field and the induction coil, mechanical energy from vibrations may be converted into electricity using the method known as the electromagnetic mechanism [7-9]. Vibration energy harvesting has also made great use of the piezoelectric mechanism. This mechanism uses piezoelectric materials' capability to produce electricity when subjected to mechanical stress [10-12].

A parametric analysis of energy extraction from Vortex-Induced Vibration (VIV) phenomena was conducted by Barrero-Gil et al. [13]. The primary purpose was to examine how tuning factors affected the effectiveness of energy extraction

using VIV. Mass ratio, mechanical damping coefficient, and Reynolds number were among the variables studied. The maximum efficiency for given mass ratios and specific flow velocity ranges were significant findings. The investigation showed that the mass-damping parameter had an impact on efficiency, with higher Reynolds numbers generally resulting in better efficiency.

Wang et al. [14] studied energy harvesting that requires the application of synchronisation in VIV phenomena. The relationship between voltage output and vibration amplitude was described using theoretical models and numerical simulations. Under synchronisation, the findings revealed large amplitudes and voltages, with a maximum voltage of 8.42 Volts at a reduced velocity, U_R, of 5.6.

Zhang et al. [15] investigated FIV numerically using two square-shaped cylinders that were interconnected in a straight line. The findings revealed that mild lock-in occurrences occurred in every instance. At $L/D = 2.0$, all flow configurations displayed a "2S" or two single vortex modes, and the dynamic response was less than that of a stationary cylinder. The oscillation amplitude increased significantly at $L/D = 6.0$ due to the interaction between the flow and the cylinders.

Several studies have investigated the FIV implementation for energy harvesting. However, the study of the effect of the combination of Reynolds number and damping ratio for harnessing the energy of circular cylinders is largely unaddressed. In this study, we aim to investigate the effects of Reynolds number ($Re = \rho U_\infty D/\mu$), reduced velocity ($U_R = U_\infty/f_n D$), and damping ratio (ζ) on the behaviour of a specific system. This study focused on a wide range of Reynolds numbers, spanning from 100 to 500. Additionally, we varied the reduced velocity within the range of 1.0 to 15.0.

Finally, three different damping ratios, namely 0.05, 0.1, and 0.5, were utilised in our investigations. By conducting numerical investigations and analysing the resulting data, we aim to gain a comprehensive understanding of how these parameters interact and influence the system's dynamics. The outcomes of this research would contribute to the existing body of knowledge in the field and potentially lead to practical applications of VEH.

2. Methods

2.1. Numerical method

The approach detailed in this section was executed through the utilisation of a numerical code built on the Fortran programming language. This code was specifically built to solve both fluid flow and structural dynamic motion. The code is composed of three essential components: pre-processing, solver, and post-processing. These components were compiled into a single program capable of generating a mesh during the pre-processing stage, solving fluid and structural dynamic problems during the solver phase, and ultimately saving the obtained results into files during the post-processing phase.

A fundamental equation that is utilised to guarantee that mass is conserved is the continuity equation. In a two-dimensional domain, the continuity equation for incompressible fluids is mathematically represented as Eq. (1).

$$\nabla \cdot u = 0 \tag{1}$$

The momentum equation is a fundamental equation that is used to ensure that the momentum of a fluid is conserved. In the context of Eulerian grid-based computations, where incompressibility is assumed, the momentum equation is written as Eq. (2).

$$\frac{\partial u}{\partial t} + (u \cdot \nabla)u = -\frac{\nabla p}{\rho} + \frac{1}{Re}\nabla^2 u + f \tag{2}$$

In order to obtain the initial acceleration for the first intermediate velocity, it is necessary to combine the convective and diffusive terms in the momentum equation. This can be done by making a summation of the terms according to Eq. (3).

$$\frac{\partial u^*}{\partial t} = -(u \cdot \nabla)u + \frac{1}{Re}\nabla^2 u \tag{3}$$

In order to obtain the first intermediate velocity, a temporal integration is implemented in Eq. (3), explicitly employing the third-order Adams-Bashforth scheme as specified in Eq. (4).

$$u^* = u^n + \Delta t \left[\frac{23}{12} a^n - \frac{16}{12}a^{n-1} + \frac{5}{12}a^{n-2}\right] \tag{4}$$

In the context provided, the temporal increment, Δt, is employed in the calculation of the first intermediate velocity (u^*). This calculation encompasses the rate of change of u^* at the current time step (a^n), the previous time step (a^{n-1}), and the time step before that (a^{n-2}). However, the first intermediate velocity does not yet fulfil the condition of being divergence-free. Therefore, to obtain the second intermediate velocity, the Poisson equation denoted in Eq. (5) is used to obtain the pressure.

$$\frac{\nabla \cdot u^*}{\Delta t} = \frac{\nabla^2 p^{t+1}}{\rho} \tag{5}$$

The determination of the second intermediate velocity, u^{**}, is achieved by utilising Eq. (6).

$$u^{**} = u^* - \frac{\Delta t}{\rho}\nabla p \tag{6}$$

After solving Eq. (6), with the use of the Direct Forcing Immersed Boundary (DFIB) method the subsequent velocity at the next time step, u^{t+1}, can be obtained by incorporating a virtual force term, as depicted in Fig. 1. This is accomplished by employing Eq. (7) in the momentum equation.

$$f^{t+1} = \eta \frac{u_s - u^{**}}{\Delta t} \tag{7}$$

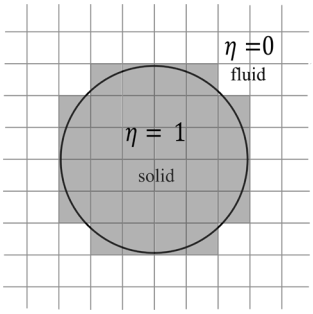

Fig. 1. Discrete cell of the DFIB method on a cartesian mesh.

In the context of the DFIB method, the quantity f^{t+1} represents the virtual force, which is added to the momentum equation to account for the effects of the numerical forcing term. The solid-body velocity vector, u_s, denotes the velocity of the solid boundary within the fluid domain, and the solid-body function, η, indicates whether a given point is in a solid or a fluid region. The velocity u^{**} is updated to u^{t+1} by employing Eq. (8), which describes the incorporation of the virtual force into the momentum equation.

$$u^{t+1} = u^{**} + \Delta t f^{t+1} \tag{8}$$

The transverse motion of the cylinders is governed by a distinct differential equation. This equation is given in Eq. (9) [16], which captures the dynamic behaviour of the cylinders. The equation is implemented after the fluid simulation is finished.

$$\ddot{y} + \frac{4\pi\zeta}{U_R}\dot{y} + \frac{4\pi^2}{(U_R)^2}y = \frac{2C_L}{\pi\, m^*} \tag{9}$$

The lift force coefficient, C_L, represents the non-dimensional lift force which is described as Eqs. (10) and (11).

$$F_y = \iiint f_y dV \tag{10}$$

$$C_L = \frac{2F_y}{\rho U_\infty^2 D} \tag{11}$$

The temporal integration to obtain velocity and displacement of the cylinder, the Dormand-Prince method [17] is implemented. By employing the Dormand-Prince method, the function evaluation of each stage is calculated based on formulae represented by a group of equations in Eq. (12).

$$\begin{aligned}
k_1 &= \Delta t\, f(t, \dot{y}) \\
k_2 &= \Delta t\, f\left(t + \frac{1}{5}\Delta t, \dot{y} + \frac{1}{5}k_1\right) \\
k_3 &= \Delta t\, f\left(t + \frac{3}{10}\Delta t, \dot{y} + \frac{3}{40}k_1 + \frac{9}{40}k_2\right) \\
k_4 &= \Delta t\, f\left(t + \tfrac{4}{5}\Delta t, \dot{y} + \tfrac{44}{45}k_1 - \tfrac{56}{15}k_2 + \tfrac{32}{9}k_3\right) \\
k_5 &= \Delta t\, f\left(t + \frac{8}{9}\Delta t, \dot{y} + \frac{19372}{6561}k_1 - \frac{25360}{2187}k_2 + \frac{64448}{6561}k_3 - \frac{212}{729}k_4\right) \\
k_6 &= \Delta t\, f\left(t + \Delta t, \dot{y} + \frac{9017}{3168}k_1 - \frac{355}{33}k_2 + \frac{46732}{5247}k_3 + \frac{49}{176}k_4 - \frac{5103}{18656}k_5\right) \\
k_7 &= \Delta t\, f\left(t + \Delta t, \dot{y} + \frac{35}{384}k_1 + \frac{500}{1113}k_3 + \frac{125}{192}k_4 - \frac{2187}{6784}k_5 + \frac{11}{84}k_6\right) \\
y_{n+1} &= y_n + \frac{35}{384}k_1 + \frac{500}{1113}k_3 + \frac{125}{192}k_4 - \frac{2187}{6784}k_5 + \frac{11}{84}k_6
\end{aligned} \tag{12}$$

The potential of extracted power is equivalent to the rate change of dissipated energy on the Power Take Off (PTO) system. The non-dimensional extracted power is given by Eq. (13) according to Soti et al. [16].

$$P = \frac{2\pi^2 m^* \zeta}{U_R}\dot{y}^2 \tag{13}$$

2.2. Computational domain

Figure 2 shows the size of the computational domain used in the simulation of the flow around a circular cylinder. The domain is rectangular, with dimensions of 40 D × 20 D, where D is the diameter of the cylinder. The cylinder is located at 15 D from the left boundary of the domain, and the flow is simulated in two dimensions. The figure represents the location of the computational domain. The domain is located in a region where the flow is relatively uniform.

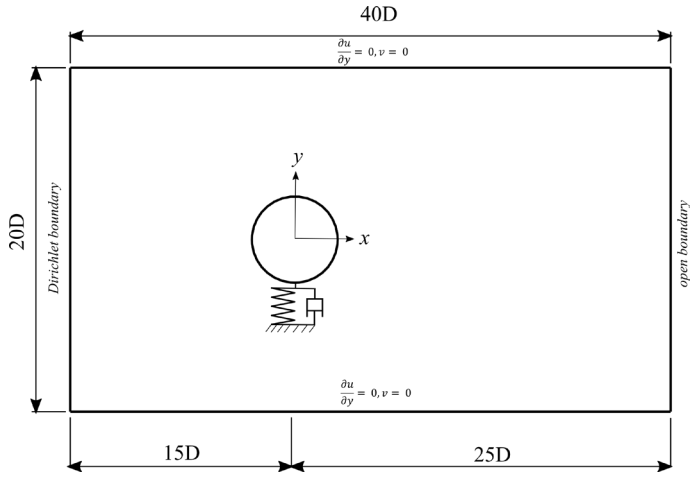

Fig. 2. Computational domain of the numerical study.

An axisymmetric boundary condition was applied to both the upper and lower sides of the computational domain. To ensure a robust representation of the flow dynamics, we employed the Dirichlet-velocity boundary condition along the left side of the domain, designated as the inlet boundary, complete with predetermined values tailored to the specific requirements of our simulation. On the right side of the domain, we established an open boundary condition, designating it as the outlet boundary.

The computational domain transformed into a non-uniform Cartesian staggered mesh. The Direct Forcing Immersed Boundary (DFIB) method was adeptly incorporated into the governing equation to ensure that the fluid adheres to the no-slip boundary condition, facilitating an accurate representation of the physical system's behaviour. This meshing strategy is illustrated in Fig. 3, showcasing the generated mesh that forms the foundation of our computational analysis.

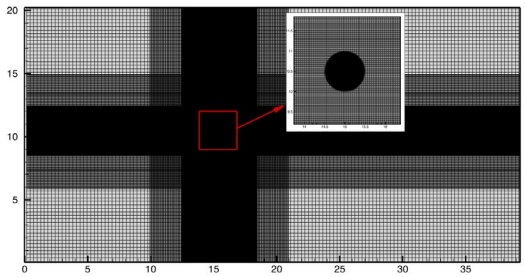

Fig. 3. Non-uniform cartesian mesh with DFIB implementation.

3. Results and Discussions

3.1. Mesh independence and validation of the numerical scheme

The parameter that reflects the computational domain resolution is the ratio of the cylinder diameter to the spacing between mesh nodes, denoted as D/dp. To determine the most suitable parameter that balances computational efficiency and accuracy, we conducted an independence study. Four different mesh resolutions were examined at D/dp equal to 20, 25, 40, and 50. The results are presented in Table 1. The independence study reveals that the difference in results between $D/dp = 40$ and $D/dp = 50$ is minimal, at 0.22%. Consequently, we selected a mesh resolution of $D/dp = 40$.

Table 1. Mesh independence.

D/dp	20	25	40	50
C_L	0.6965	0.70475	0.686	0.6845

Figure 4 shows the time history of the lift force coefficient (C_L) and corresponding frequency response at $Re = 100$ and $Re = 200$. Tables 2 and 3 show the validation data obtained from Fig. 4. The tables compare these results with findings from other studies. The validation data, which represents the force coefficient of the flow to the cylinder, were measured by the drag (C_D), lift coefficients (C_L) and Strouhal number ($\mathrm{St} = fD/U_\infty$), where f represents the vortex shedding frequency and U_∞ represents free stream fluid velocity.

By accurately capturing the drag and lift coefficients, the method demonstrates its ability to effectively model and analyse the intricate interactions in such fluid flow scenarios. As a result, this study is able to confidently rely on this numerical method as a tool to study and comprehend flow phenomena involving circular cylinders.

Table 2. Flow past a circular cylinder in uniform flow data comparison of C_D, C_L and Strouhal Number (St) at $Re = 100$ with the benchmark data.

Data ($Re = 100$)	C_D (average)	C_L (RMS)	C_L (peak)	St
Present study	1.3550	0.2215	0.3330	0.1697
Noor et al. [18]	1.4000			0.1670
Su et al. [19]	1.4000		0.3400	0.1680
Rajani et al. [20]	1.3353	0.1802		0.1569
Qu et al. [21]	1.3170	0.2224		0.1649
Kadapa et al. [22]			0.3380	0.1690

Table 3. Flow past a circular cylinder in uniform flow data comparison of C_D, C_L and Strouhal Number (St) at $Re = 200$ with the benchmark data.

Data ($Re = 200$)	C_D (average)	C_L (RMS)	C_L (peak)	St
Present study	1.348	0.471	0.686	0.2002
Rajani et al. [20]	1.3365	0.4276		0.1957
Qu et al. [21]	1.316	0.4678		0.1958
Kadapa et al. [22]			0.689	0.202

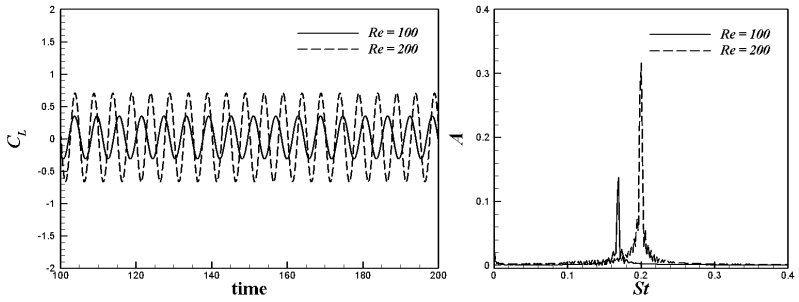

Fig. 4. Time history of lift force coefficient (C_L) and corresponding frequency response.

3.2. Parameters study

3.2.1. The effects of parameters on cylinder displacement

Figure 5 displays the time series of the cylinder's non-dimensional displacement under certain parameters, namely $U_R = 6.0$ and 0.5. The colours of the lines in the illustration correspond to different Reynolds numbers ranging from 100 to 500. Analysing the dynamic response of the cylinder, as shown in Fig. 5, reveals that the magnitude of the non-dimensional displacement grows progressively with increasing Reynolds numbers except for Re = 400 where it decreases. Examining the patterns in Fig. 5, we can see that as the Reynolds number increases, there is a distinct amplification in the magnitude of the displacement.

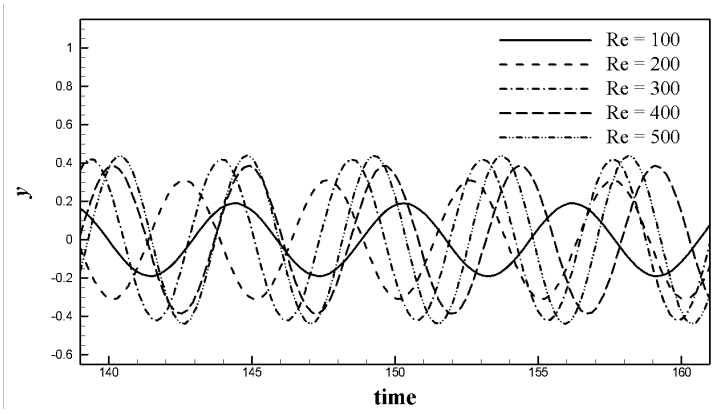

Fig. 5. Time history of non-dimensional displacement at $U_R = 6.0$ and $\zeta = 0.5$.

Figure 6 provides comprehensive insights into the behaviour of the cylinder motion in the frequency domain by illustrating the magnitude of amplitude at different frequencies. Upon a thorough analysis of Fig. 6, a clear and consistent pattern emerges where an increase in the Reynolds number corresponds to a discernible increase in the fundamental frequency of the cylinder motion. The fundamental frequency, which represents the primary and dominant oscillation frequency of the cylinder, plays a pivotal role in characterising the dynamic behaviour of the system.

Upon careful examination of Fig. 6, a clear and a trend emerges, revealing that with increasing Reynolds numbers, there is a discernible escalation in the fundamental frequency, thereby indicating a notable shift towards higher oscillation rates characterised by faster rate change of displacement.

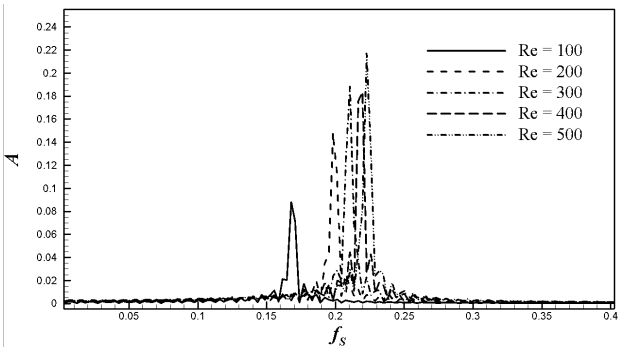

Fig. 6. Frequency response of displacement amplitude at U_R= 6.0 and $\zeta = 0.5$.

Figure 7 provides detailed insights into the influence of U_R (reduced velocity) and ζ (damping ratio) on the root mean square (RMS) of the non-dimensional displacement of the cylinder (y_{RMS}) under various Reynolds numbers (Re). This figure allows for a comprehensive analysis of the relationship between these parameters and the magnitude of y_{RMS}.

Upon analysing Fig. 7, it becomes evident that, regardless of the specific combination of U_R and ζ, the y_{RMS} consistently increases with the increase in U_R until it reaches a peak magnitude. This peak indicates the optimal relation between parameters, resulting in the maximum displacement of the cylinder. Beyond this peak, further increases in U_R may lead to the reduction of y_{RMS} magnitude. This behaviour is consistent with the finding of Leontini et al. [23] and Soti et al. [16].

At a Re = 100, y_{RMS} exhibits interesting trends for different values of the damping coefficient ζ. Specifically, when ζ = 0.1, the y_{RMS} reaches its highest peak value, surpassing the values observed for other damping coefficients. Following this, for ζ = 0.5, the y_{RMS} has a comparatively lowest peak value.

Examining the y_{RMS} behavior for ζ = 0.05 and 0.1 in two distinct U_R ranges, namely 1.0<U_R<3.0 and 12.0<U_R<15.0, reveals an intriguing observation. The corresponding y_{RMS} lines for these two damping coefficients nearly coincide within these U_R intervals, implying a similarity in their magnitudes. This suggests that, under these specific conditions, the effect of the damping coefficient on the y_{RMS} is relatively insignificant.

However, an interesting phenomenon occurs in the range of 4.0<U_R<5.0, where a sudden and significant increase in the y_{RMS} magnitude is observed. This abrupt change in y_{RMS} is noticeable for both ζ = 0.5 and ζ = 0.1. Conversely, a sudden decrease in y_{RMS} occurs within the range of 7.0<U_R<8.0, again observed for both ζ = 0.5 and ζ = 0.1.

Notably, the absence of such sudden increases or decreases in y_{RMS} for ζ = 0.5 indicates that it possesses a more substantial damping force in comparison to the aforementioned damping coefficients. This suggests that the damping

characteristics associated with ζ = 0.5 play a significant role in stabilising the system and reducing the occurrence of large fluctuations in y_{RMS}.In the reduced velocity range spanning from 8.0 <U_R <15.0, a noteworthy observation emerges regarding the y_{RMS} magnitude when subjected to a damping ratio of ζ = 0.5. Specifically, it becomes evident that the y_{RMS} assumes a substantially larger amplitude in comparison to the alternative damping ratios under consideration.

When examining the behaviour of y_{RMS} at Re = 200 and 500, a remarkable similarity in the trends governing the magnitude of this variable becomes apparent. Both Re values exhibit comparable patterns, suggesting a consistent dynamic behaviour of y_{RMS} across different Reynolds numbers. However, a slight discrepancy arises when considering the peak values of y_{RMS} for the two Reynolds numbers.

At Re = 500, the peak value of y_{RMS} surpasses that observed at Re = 200, indicating a higher amplitude of y in the former case. This difference suggests that at higher Reynolds numbers, the fluctuations in the variable y become more pronounced, leading to an increase in the peak value of y_{RMS}. Moreover, the occurrence of these peak values also diverges in terms of the corresponding U_R ranges.

At Re = 200, the peak values of y_{RMS} manifest at a velocity range of $U_R = 6.0$, indicating a critical point where the amplitude of y reaches its maximum. On the other hand, at Re = 500, these peak values occur at a slightly lower U_R range, specifically at $U_R = 5.0$. This suggests that the dynamics of y, as captured by y_{RMS}, exhibit variations to the Reynolds number, leading to discrepancies in the magnitudes and occurrence of peak values.

Interestingly at Re = 300 and 400 the peak values of y_{RMS} have similar patterns. The highest peak value happened at the lowest damping ratio ζ = 0.05 and the lowest peak value happened at the highest damping ratio ζ = 0.5. They also happen at the same reduced velocity at $U_R = 4.0$ with the exception of ζ = 0.5 with Re = 300, it happens at $U_R = 7.0$.

It is appealing that, at Re = 300 and 400, a distinct and notable similarity emerges in the pattern exhibited by the peak values of y_{RMS}. Strikingly, regardless of the specific Re considered, the highest peak value of y_{RMS} consistently occurs when the damping ratio assumes its lowest value at ζ = 0.05, while the lowest peak value is consistently observed when ζ reaches its highest value of 0.5. This intriguing relationship between the damping ratio and the magnitude of y_{RMS} suggests that the degree of damping has a profound influence on the oscillatory behavior and energy dissipation within the system.

Furthermore, the peak values of y_{RMS} at Re = 300 and 400 are found to occur at the same reduced velocity, namely $U_R = 4.0$, except for the case where ζ = 0.5 and Re = 300, where the peak value is instead observed at $U_R = 7.0$. This discrepancy highlights the subtle relation between the damping ratio, Reynolds number, and the reduced velocity range at which the system exhibits its maximum amplitude.

Taken together, these findings from Fig. 7 provide insights into the intricate dynamics of the system under investigation, comprehensively explained the influence of damping, Reynolds number, and reduced velocity on the magnitude and occurrence of y_{RMS}.

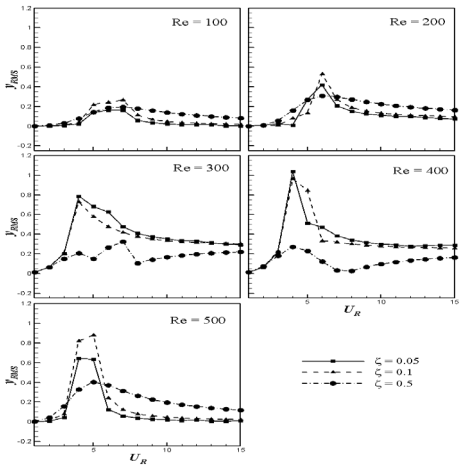

Fig. 7. Root mean square (RMS) of non-dimensional displacement of the cylinder with the variations of U_R, ζ, and Reynolds numbers.

3.2.2. The effect of parameters on potential generated power

Figure 8 presents a detailed view of the average potential generated power (P_{AVG}) for U_R, Re, and ζ. The graph provides a comprehensive insight into the relationships between these variables and how they impact power generation. In general, we observe a discernible trend where P_{AVG} tends to increase as U_R increases. This trend continues until it reaches a maximum value, after which P_{AVG} starts to decrease with further increases in U_R. This phenomenon was also observed in study by Wang et al. [24].

However, it is important to note that within a certain range of U_R, there are notable exceptions to this general trend. In this specific range, we observe a sharp decrease in P_{AVG}, deviating from the overall increasing pattern. This unexpected decline in power generation within this particular U_R range suggests the presence of influencing factors that counteract the anticipated increase. Furthermore, it is noteworthy that after this range of sharp decrease, there is a subsequent increase in P_{AVG}. This observed increase occurs at specific U_R values, particularly at $\zeta = 0.5$.

These fluctuations of P_{AVG}, occurring within the specified U_R range, exhibit interesting patterns across various corresponding Re values. Notably, when ζ is set to 0.5, these fluctuations are observed across the entire range of Re values. Additionally, when ζ is set to 0.1 and Re are fixed at 200 and 400, similar fluctuations also manifest. Moreover, the degree of fluctuation varies among different Re values, with the most significant fluctuation occurring at Re = 200. This observation suggests that Re = 200 represents a particularly critical point where P_{AVG} experiences the largest magnitude of variations.

The peak value of P_{AVG} exhibits variations based on Re and ζ at all corresponding U_R. When analysing the data, it becomes evident that the highest peak value of P_{AVG} occurs at Re = 400. This indicates that the system achieves the maximum power generation capacity at this specific Re. Following $Re = 400$, the next highest peak value is observed at $Re = 300$, suggesting a slightly lower but still significant power generation capability. Subsequently, $Re = 500$ exhibits a

peak value lower than Re $= 300$ but higher than Re $= 200$ and Re $= 100$, which demonstrates a decreasing trend in power generation as Re decreases.

Finally, Re $= 200$ and Re $= 100$ represent the lowest peak values of P_{AVG} among the tested Reynolds numbers, indicating relatively lower power generation efficiency in those cases. These findings emphasise the critical influence of Re on, with $Re = 400$ showcasing the highest P_{AVG} and subsequent reductions in peak values as Re decreases. Figure 8 also shows that the peak P_{AVG} at each Re happened at $\zeta = 0.5$. It occurs due to the largest dissipated energy by the VEH at the highest damping ratio $\zeta = 0.5$.

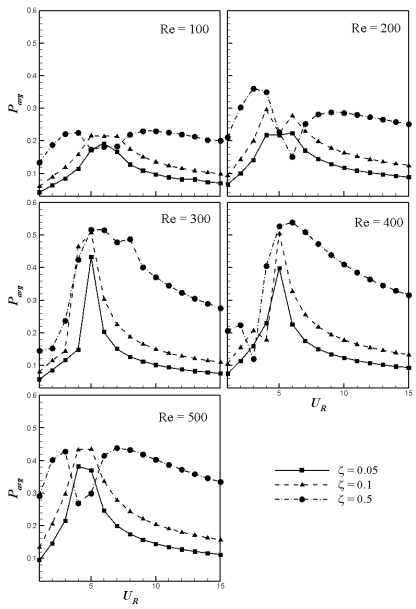

Fig. 8. Average value of non-dimensional potential power harvested by the cylinder with the variations of reduced velocity (U_R), damping ratio (ζ), and Reynolds number (Re).

4. Conclusions

In conclusion, the analysis of the numerical data reveals insights into the behaviour of the system under investigation. The dynamic response of the cylinder shows that the non-dimensional displacement increases with increasing Reynolds numbers, except for $Re = 400$ where it decreases. The patterns indicate that as the Reynolds number increases, there is a distinct amplification in the magnitude of the displacement. The behavior of the cylinder motion in the frequency domain indicates that an increase in the Reynolds number corresponds to a discernible increase in the fundamental frequency of the cylinder motion. This trend signifies a notable shift towards higher oscillation rates characterised by faster rate changes of displacement.

The root mean square (RMS) of the non-dimensional displacement of the cylinder (y_{RMS}) consistently increases with increasing reduced velocity (U_R) until it reaches a peak magnitude. Beyond this peak, further increases in U_R may lead to

a reduction in the y_{RMS} magnitude. Additionally, the damping ratio (ζ) influences the y_{RMS} magnitude, with $\zeta = 0.1$ resulting in the highest peak value and $\zeta = 0.5$ yielding the lowest peak value. Notably, sudden increases and decreases in y_{RMS} are observed within specific U_R ranges and the absence of such fluctuations for $\zeta = 0.5$ indicates its stronger damping characteristics.

The average potential generated power (P_{AVG}) for variation of U_R, Re, and ζ have already been analysed. Generally, P_{AVG} increases with U_R until it reaches a maximum value, after which it decreases with further increases in U_R. However, there are exceptions within a specific U_R range, where a sharp decrease in P_{AVG} is observed. This decline is followed by a subsequent increase in P_{AVG} at specific U_R values, particularly at $\zeta = 0.5$. The fluctuations in P_{AVG} are observed across various Re values, with the most significant variation occurring at $\mathrm{Re} = 200$. Furthermore, the peak value of P_{AVG}, exhibit variations based on Re and ζ, with $\mathrm{Re} = 400$ yielding the highest peak value.

Nomenclatures

a	Intermediate velocity rate of change
C_D	Drag coefficient
C_L	Lift coefficient
D	Diameter of the cylinder
dp	Distance between mesh node
F_y	Transverse force
f	Virtual force
f_n	Structure natural frequency
f_S	Structure frequency
f_y	Virtual force in transverse direction
m^*	The mass ratio of solid to the displaced fluid
n	Time step level
P	Power generated
p	Fluid pressure
P_{avg}	The average of power generated
Re	Reynolds number
St	Strouhal number
t	Time
u	Velocity vector
u^*	First intermediate velocity vector
u^{**}	Second intermediate velocity vector
u_s	Solid/ structure velocity vector
V	Volume of solid
U_R	Reduced velocity
U_∞	Free stream velocity
y	Cylinder displacement
y_{max}	Amplitude of cylinder displacement
y_{RMS}	Root mean square of cylinder displacement
$\dot{y}$	Cylinder velocity
$\ddot{y}$	Cylinder acceleration

Greek Symbols

ρ	The density of the fluid
η	The volume of solid function
ζ	The damping ratio

Abbreviations

DFIB	Direct forcing immersed boundary.
FIV	Flow-induced vibration
VEH	Vibration energy harvesting
VIV	Vortex-induced vibration

References

1. Pan, H.; Qi, L.; Zhang, Z.; and Yan, J. (2021). Kinetic energy harvesting technologies for applications in land transportation: A comprehensive review. *Applied Energy*, 286, 116518.
2. An-Nizhami, A.; Apriandi, N.; Yanuar, P.; and Nugroho, W.I. (2022). Pemodelan sistem suspensi pasif dan semi aktif regeneratif dengan model half car dan eksitasi harmonik. *Jurnal Rekayasa Mesin*, 17(2), 297-306.
3. An-Nizhami, A.; and Riadini, E.R. (2021). Analisa numerik pengaruh karakteristik gelombang air laut pada wave energy converter tipe bottom hinge menggunakan metode smoothed particles hydrodynamics. *Jurnal Rekayasa Mesin*, 16(1), 32-38.
4. Lin, Z.; and Zhang, Y. (2016). Dynamics of a mechanical frequency up-converted device for wave energy harvesting. *Journal of Sound and Vibration*, 367, 170-184.
5. Sardini, E.; and Serpelloni, M. (2010). Self-powered wireless sensor for air temperature and velocity measurements with energy harvesting capability. *IEEE Transactions on Instrumentation and Measurement*, 60(5), 1838-1844.
6. Sebald, G.; Guyomar, D.; and Agbossou, A. (2009). On thermoelectric and pyroelectric energy harvesting. *Smart Materials and Structures*, 18(12), 125006.
7. Yang, T.; and Cao, Q. (2020). Dynamics and high-efficiency of a novel multi-stable energy harvesting system. *Chaos, Solitons and Fractals*, 131, 109516.
8. Maamer, B.; Boughamoura, A.; El-Bab, A.M.R.F.; Francis, L.A.; and Tounsi, F. (2019). A review on design improvements and techniques for mechanical energy harvesting using piezoelectric and electromagnetic schemes. *Energy Conversion and Management*, 199(1), 111973.
9. Aouali, K.; Kacem, N.; Bouhaddi, N.; and Haddar, M. (2021). On the optimization of a multimodal electromagnetic vibration energy harvester using mode localization and nonlinear dynamics. *Actuators*, 10(2), 25.
10. Mutsuda, H.; Tanaka, Y.; Patel, R.; and Doi, Y. (2017). Harvesting flow-induced vibration using a highly flexible piezoelectric energy device. *Applied Ocean Research*, 68, 39-52.
11. Qian, F.; Liao, Y.; Zuo, L.; and Jones, P. (2021). System-level finite element analysis of piezoelectric energy harvesters with rectified interface circuits and experimental validation. *Mechanical Systems and Signal Processing*, 151, 107440.

12. Tran, N.; Ghayesh, M.H.; and Arjomandi, M. (2018). Ambient vibration energy harvesters: A review on nonlinear techniques for performance enhancement. *International Journal of Engineering Science*, 127, 162-185.
13. Barrero-Gil, A.; Pindado, S.; and Avila, S. (2012). Extracting energy from vortex-induced vibrations: A parametric study. *Applied Mathematical Modelling*, 36(7), 3153-3160.
14. Wang, J.; Ran, J.; and Zhang, Z. (2014). Energy harvester based on the synchronisation phenomenon of a circular cylinder. *Mathematical Problems in Engineering*, 2014, 1-9.
15. Zhang, H.; Zhou, L.; and Tse, T.K.T. (2022). Mode-based energy transfer analysis of flow-induced vibration of two rigidly coupled tandem cylinders. *International Journal of Mechanical Sciences*, 228(12), 107468.
16. Soti, A.K.; and De, A. (2020). Vortex-induced vibrations of a confined circular cylinder for efficient flow power extraction. *Physics of Fluids*, 32(3), 033603.
17. Dormand, J.R.; and Prince, P.J. (1980). A family of embedded Runge-Kutta formulae. *Journal of Computational and Applied Mathematics*, 6(1), 19-26.
18. Noor, D.Z.; Chern, M.J.; and Horng, T.L. (2009). An immersed boundary method to solve fluid-solid interaction problems. *Computational Mechanics*, 44(4), 447-453.
19. Su, S.W.; Lai, M.C.; and Lin, C.A. (2007). An immersed boundary technique for simulating complex flows with rigid boundary. *Computers & Fluids*, 36(2), 313-324.
20. Rajani, B.N.; Kandasamy, A.; and Majumdar, S. (2009). Numerical simulation of laminar flow past a circular cylinder. *Applied Mathematical Modelling*, 33(3), 1228-1247.
21. Qu, L.; Norberg, C.; Davidson, L.; Peng, S.H.; and Wang, F. (2013). Quantitative numerical analysis of flow past a circular cylinder at Reynolds number between 50 and 200. *Journal of Fluids and Structures*, 39, 347-370.
22. Kadapa, C.; Dettmer, W.G.; and Perić, D. (2020). Accurate iteration-free mixed-stabilised formulation for laminar incompressible Navier-Stokes: Applications to fluid-structure interaction. *Journal of Fluids and Structures*, 97, 103077.
23. Leontini, J.S.; Thompson, M.C.; and Hourigan, K. (2006). The beginning of branching behaviour of vortex-induced vibration during two-dimensional flow. *Journal of Fluids and Structures*, 22(6-7), 857-864.
24. Wang, J.; Sun, S.; Tang, L.; Hu, G.; and Liang, J. (2021). On the use of metasurface for Vortex-Induced vibration suppression or energy harvesting. *Energy Conversion and Management*, 235(4), 113991.